JOURNAL OF PROPULSION AND POWER
Vol. 14, No. 5, September–October 1998

Modeling High-Pressure Mixing and Combustion Processes in Liquid Rocket Engines

Joseph C. Oefelein* and Vigor Yang†
Pennsylvania State University, University Park, Pennsylvania 16802

Modeling high-pressure mixing and combustion processes in liquid rocket engines involves a variety of challenges that include all of the classical closure problems and a unique set of problems imposed by the introduction of thermodynamic nonidealities and transport anomalies. The complicating factors of chemical kinetics, highly nonlinear source terms, and subgrid-scale velocity and scalar-mixing interactions must all be considered. The situation becomes more complex with increasing pressure because of an inherent increase in the flow Reynolds number and difficulties that arise when fluid states approach the critical condition. This paper 1) outlines the fundamental difficulties associated with modeling mixing and combustion processes at near-critical conditions, 2) outlines the theoretical and numerical framework developed to handle these difficulties, and 3) presents the results of simulations that lend insight into the intricate nature of the problem. Case studies focus on model performance and accuracy requirements, Lagrangian–Eulerian treatments of transcritical spray dynamics, and pure Eulerian treatments of transcritical and supercritical mixing and combustion processes.

Introduction

MODELING near-critical mixing and combustion processes numerically poses a variety of challenges that include all of the classical closure problems and a unique set of problems imposed by the introduction of thermodynamic nonidealities and transport anomalies. From the classical point of view, reacting, multiphase flows introduce the complicating factors of chemical kinetics, highly nonlinear source terms, and a variety of subgrid-scale (*sgs*) velocity and scalar-mixing interactions. Flowfield evolution is affected by compressibility effects (volumetric changes induced by changes in pressure) and variable inertia effects (volumetric changes induced by variable composition and/or heat addition). The resultant coupling dynamics yield an array of fluid dynamic and physicochemical processes that are dominated by widely disparate time and length scales, many being smaller than can be resolved in a numerically feasible manner. The situation becomes more complex with increasing pressure because of an inherent increase in the flow Reynolds number, which characterizes a further decrease in the scales associated with *sgs* interactions and difficulties that arise when fluid states approach the critical condition. Near the critical point, propellant mixture properties exhibit liquid-like densities, gas-like diffusivities, and pressure-dependent solubilities. Surface tension and heat of vaporization approach zero, and the isothermal compressibility and constant pressure specific heat increase significantly. These phenomena, coupled with extreme local property variations, have a significant impact on the evolutionary dynamics exhibited by a given system.

Experimental efforts to characterize propellant injection, mixing, and combustion processes at near-critical conditions have only recently led to a better qualitative understanding of the mechanisms involved.[1–4] The current database, however, is not adequate with respect to quantitative assessments, and theoretical efforts are similarly deficient because of a lack of validated theories, difficulties associated with numerical robustness, and limited computational capacities. Depending on the injector type, fluid properties, and flow characteristics, two limiting extremes may be deduced. At subcritical chamber pressures, injected liquid jets undergo the classical cascade of processes associated with atomization. For this situation, dynamic forces and surface tension promote the formation of a heterogeneous spray that evolves continuously over a wide range of thermophysical regimes. As a consequence of this, spray flames form and are lifted away from the injector face in a manner consistent with the combustion mechanisms exhibited by local droplet clusters. When chamber pressures approach or exceed the critical pressure of a particular propellant, however, injected liquid jets undergo a "transcritical" change of state as interfacial fluid temperatures rise above the saturation or critical temperature of the local mixture. For this situation, diminished intermolecular forces promote diffusion-dominated processes prior to atomization and respective jets vaporize, forming a continuous fluid in the presence of exceedingly large gradients. Well-mixed diffusion flames evolve and are anchored by small but intensive recirculation zones generated by the shear layers imposed by adjacent propellant streams. These flames produce wakes that extend far downstream.

Figure 1 illustrates the basic phenomena just described for the case of a liquid-oxygen–gaseous-hydrogen shear-coaxial injector element. The flow visualization studies conducted by Mayer and Tamura[1] demonstrated the dramatic effect of pressure on mixing and combustion processes within this type of injector. When the liquid-oxygen is injected at low-subcritical pressures (see Table 1), jet atomization occurs forming a distinct spray similar to that depicted in Fig. 1a. Ligaments are detached from the jet surface, forming spherical droplets, which subsequently break up and vaporize. As the chamber pressure approaches the thermodynamic critical pressure of oxygen, the number of droplets present diminishes and the situation depicted in Fig. 1b dominates. For this situation, thread-like structures evolve from the liquid core and diffuse rapidly within the shear layer induced by the coflowing jets. At a downstream distance of approximately 50 diameters, the dense fluid core breaks into "lumps," which are of the same order of magnitude as the diameter of the liquid-oxygen jet.

Received Oct. 21, 1997; revision received June 24, 1998; accepted for publication June 25, 1998.

*Research Associate, Department of Mechanical Engineering; currently at Stanford University, Department of Mechanical Engineering, Building 500, Room 501I, Stanford, CA 94305-3030. E-mail: jco@stanford.edu. Senior Member AIAA.

†Professor, Department of Mechanical Engineering. E-mail: vigor@psu.edu. Associate Fellow AIAA.

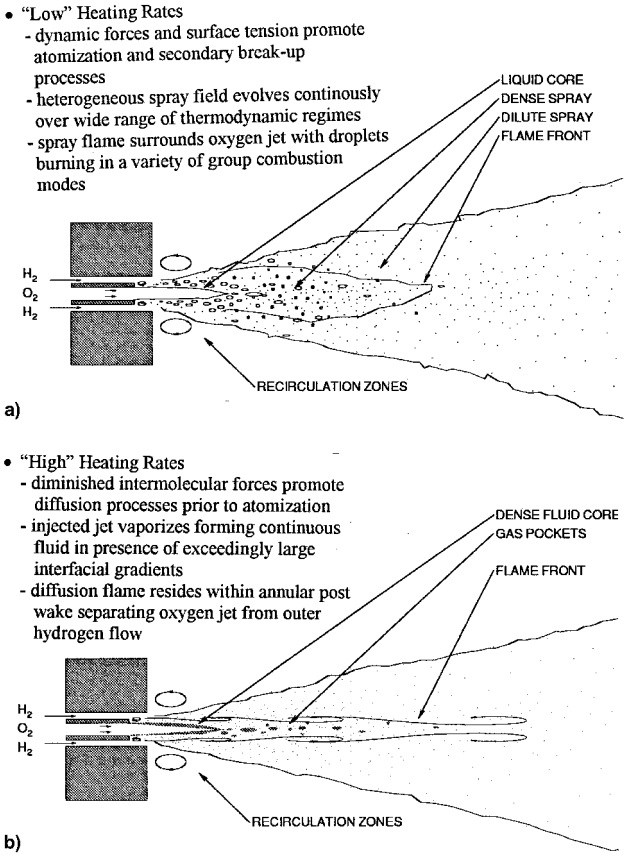

Fig. 1 Schematic diagrams illustrating the basic phenomena associated with a) low and b) high chamber pressures for the case of a liquid-oxygen–gaseous-hydrogen shear-coaxial injector element.

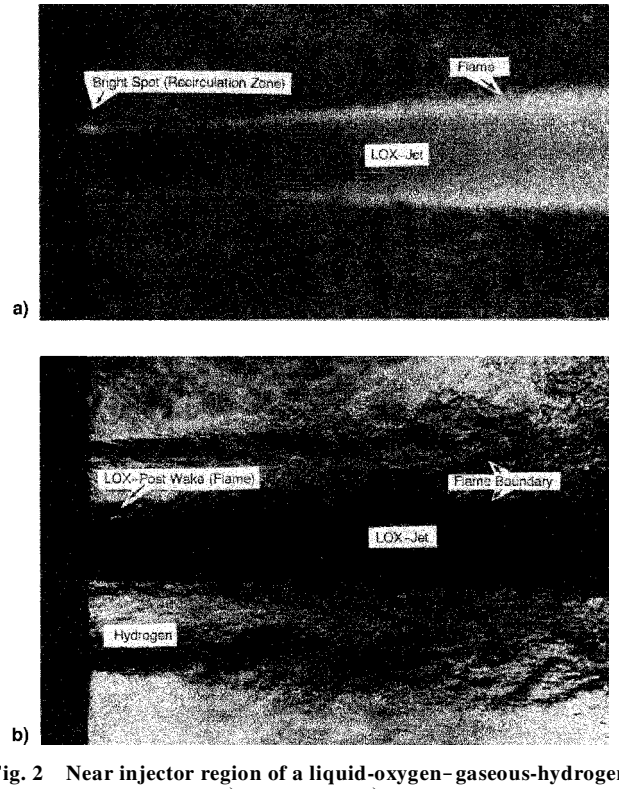

Fig. 2 Near injector region of a liquid-oxygen–gaseous-hydrogen shear-coaxial injector, a) flame and b) corresponding flowfield. Oxygen and hydrogen velocities are 30 and 300 m/s, respectively, oxygen and hydrogen injection temperatures are 100 and 300 K, oxygen, jet diameter is 1 mm, and the chamber pressure is 4.5 MPa (Mayer and Tamura[1]).

Table 1 Critical pressure and temperature of hydrogen and oxygen

	H_2	O_2
P_c	1.30 MPa (12.8 atm)	5.04 MPa (49.7 atm)
T_c	33.2 K	155 K

Results of spark photography, flame photography, and high-speed cinematography[1] reveal that flame attachment occurs instantaneously after ignition in the small but intensive recirculation zone that forms just downstream of the annular post. A well-mixed diffusion flame forms within this region, producing a wake that separates the oxygen stream from the hydrogen-rich outer flow. This wake persists at least 15 jet diameters downstream. Figure 2 shows the resultant flame structure and corresponding flowfield. Here, the injected jet exhibits a pure diffusion mechanism at a pressure of 4.5 MPa, which is slightly below the thermodynamic critical pressure of oxygen, and significantly above that of hydrogen. Hutt and Cramer[2] have reported similar findings using a swirl-coaxial configuration.

The trends outlined in the preceding text coincide with the results of high-pressure liquid-nitrogen–helium cold-flow tests conducted by Mayer et al.[3] and Woodward and Talley.[4] From a qualitative standpoint, these experiments have demonstrated the effect of mixture properties on injected liquid jets and the prevalence of one limit over the other, as illustrated in Fig. 1. The cutoff associated with these two limits, however, is not distinct and does not necessarily coincide with the critical point properties of either propellant. The dynamic forces associated with a swirl-coaxial injector, for example, would most likely dominate even under supercritical chamber conditions. For this situation, a combination of dense transcritical spray dynamics and diffusion-dominated processes would need to be considered. A shear-coaxial element, however, would be more prone to exhibit a pure diffusion mechanism. Transient conditions would alter the dynamics associated with either extreme. Thus, depending on the situation, a combination of two fundamental theoretical approaches is warranted. The first is the classical Lagrangian–Eulerian implementation in which a particulate phase is assumed to exist in the flowfield. The second employs a pure Eulerian implementation to treat a dense multicomponent fluid. Both approaches require detailed representations of mixture properties and *sgs* interactions over the full range of thermophysical regimes encountered in contemporary systems.

Several deficiencies exist with respect to the state of the art as it pertains to the theoretical treatments outlined earlier. Lagrangian tracking schemes have been proven to be efficient methodologies for modeling dilute particle distributions. Difficulties arise, however, within the dense spray regime because of a lack of information regarding jet atomization, secondary break-up processes, and appropriate combustion mechanisms. With Eulerian-based models, the issue of scale resolution and numerical diffusion must be considered to obtain solutions of flowfields with exceedingly large gradients. At 100 atm, for example, the density ratio associated with a 100 K liquid-oxygen jet and a 300 K gaseous-hydrogen stream (the conditions employed by Mayer and Tamura and representative of conditions in a liquid rocket) is approximately 144. In a shear-coaxial element, this change occurs over an interval smaller than the thickness of the annular post, which is typically on the order of 0.1 mm. Resolving numerically a gradient of this size requires the use of extremely fine grids. Because of the grid sizes required, such calculations are only now becoming feasible.

The complexity of the system outlined earlier is numerically demanding and several tradeoffs are required with respect to the hierarchy of processes and characteristic scales resolved. A variety of uncertainties exist with regard to the closure prob-

lem, and in many cases computational capacity is in direct conflict with the accuracy of the *sgs* models employed. To address these difficulties in a manner consistent with current experimental efforts, Oefelein[5] focused on detailed representations of fluid dynamic and physicochemical processes within planar mixing layers. The hydrogen–oxygen system is employed in all cases, with inlet conditions specified both with and without a splitter plate included in the flow domain. The approach follows four fundamental steps: 1) development of a general theoretical framework; 2) specification of detailed property evaluation schemes and consistent closure methodologies; 3) implementation of an efficient and time-accurate numerical framework; and 4) simulation and analysis of a systematic series of case studies that focus on model performance and accuracy requirements, Lagrangian–Eulerian treatments of transcritical spray dynamics, and pure Eulerian treatments of transcritical and supercritical mixing and combustion processes. This paper presents an overview of the theories, formulations, and key results acquired from this effort.

Theoretical and Numerical Framework

The theoretical framework developed by Oefelein accommodates dense multicomponent fluids in the Eulerian frame and dilute particle dynamics in the Lagrangian frame over a wide range of scales in a fully coupled manner. This system is obtained by filtering the small-scale dynamics from the resolved scales over a defined set of spatial and temporal intervals. Beginning with the instantaneous system, filtering is performed in two stages. First, the influences of *sgs* turbulence and chemical interactions are accounted for, yielding the well-known closure problem for turbulent reacting gases. The second filtering operation incorporates *sgs* particle interactions. With the neglect of body forces, radiation, Dufour, and Soret effects, the resultant system of Favre-filtered conservation equations of mass, momentum, total energy, and species concentration for a compressible, chemically reacting fluid composed of N species can be expressed, respectively, in conservative form as

$$\frac{\partial}{\partial t}(\theta\bar{\rho}) + \nabla\cdot(\theta\bar{\rho}\tilde{u}) = \dot{\rho}_s \tag{1}$$

$$\frac{\partial}{\partial t}(\theta\bar{\rho}\tilde{u}) + \nabla\cdot[\theta(\bar{\rho}\tilde{u}\tilde{u} + \bar{p}I)] = \nabla\cdot(\theta\bar{\tau}) - \nabla\cdot(\theta T) + \dot{F}_s \tag{2}$$

$$\frac{\partial}{\partial t}(\theta\bar{\rho}\tilde{e}_t) + \nabla\cdot[\theta(\bar{\rho}\tilde{e}_t + \bar{p})\tilde{u}] = \nabla\cdot(\theta\bar{q}_e) + \nabla\cdot(\theta\bar{\tau}\cdot\tilde{u}) - \nabla\cdot(\theta Q) - \nabla\cdot(\theta T\cdot\tilde{u}) + \dot{Q}_s \tag{3}$$

$$\frac{\partial}{\partial t}(\theta\bar{\rho}\tilde{Y}_i) + \nabla\cdot(\theta\bar{\rho}\tilde{Y}_i\tilde{u}) = \nabla\cdot(\theta\bar{q}_i) - \nabla\cdot(\theta S_i) + \theta\bar{\dot{\omega}}_i + \dot{\omega}_{s_i} \qquad i = 1, \ldots, N \tag{4}$$

where

$$\bar{\tau} = -\frac{2}{3}\bar{\rho}\nu(\nabla\cdot\tilde{u})I + \bar{\rho}\nu(\nabla\tilde{u} + \nabla\tilde{u}^T)$$

$$\tilde{e}_t = \tilde{e} + \frac{1}{2}\tilde{u}\cdot\tilde{u} + \frac{1}{2}\frac{\mathrm{tr}(T)}{\bar{\rho}}$$

$$\tilde{e} = \sum_{i=1}^{N}\tilde{h}_i\tilde{Y}_i - \frac{\bar{p}}{\bar{\rho}}$$

$$\tilde{h}_i = h_{f_i}^o + \int_{\bar{p}_{\mathrm{ref}}}^{\bar{p}}\int_{\tilde{T}_{\mathrm{ref}}}^{\tilde{T}} C_{p_i}\,\mathrm{d}T\,\mathrm{d}p$$

$$\bar{q}_e = \lambda\nabla\tilde{T} + \sum_{i=1}^{N}\overline{h_i q_i}, \qquad \bar{q}_i = \bar{\rho}\bar{\mathcal{D}}_{im}\nabla\tilde{Y}_i$$

In the preceding equations, τ represents the viscous stress tensor, e_t the total internal energy, q_e the energy flux because of heat conduction and mass diffusion, and q_i the mass diffusion flux of the ith species. The viscous stress tensor is assumed to follow Stokes' hypothesis, and Fick's and Fourier's laws have been used to approximate species and thermal diffusion processes, respectively. The quantities T, Q, S_i, and $\bar{\dot{\omega}}_i$ represent the *sgs* momentum, energy, and species fluxes and the resolved-scale chemical source terms, respectively. The terms θ, $\dot{\rho}_s$, $\dot{F}_s$, $\dot{Q}_s$, and $\dot{\omega}_{s_i}$ represent the resolved-scale void fraction induced when a spray is present and the corresponding interphase exchange functions for mass, momentum, energy, and species. A detailed derivation and description of the filtered system is given by Oefelein[5] and is also presented in Oefelein and Yang.[6]

Equations (1–4), coupled with an appropriately filtered equation of state, represent the conservation laws in an average sense based on the level of spatial and temporal resolution employed in the calculation procedure. This system is fully characterized by the resolved-scale variables $\bar{p}$, $\tilde{u}$, $\tilde{T}$, and $\tilde{Y}_1, \ldots, \tilde{Y}_N$ upon the specification of empirical or analytical models that adequately describe 1) the thermodynamic and transport properties C_p, μ, λ, and $\bar{\mathcal{D}}_{im}$; 2) the *sgs* interactions represented by T, Q and S_i; 3) the *sgs* particle interactions represented by θ, $\dot{\rho}_s$, $\dot{F}_s$, $\dot{Q}_s$, and $\dot{\omega}_{s_i}$; and 4) the resolved-scale chemical kinetics represented by $\bar{\dot{\omega}}_i$. The resultant system of integro-differential equations provides a unified framework that facilitates the closure problem in a well-posed, numerically compatible manner.

Modeling *sgs* phenomena poses stringent numerical demands, and robust models are currently beyond the state of the art. Because of the uncertainties associated with the current models and the intensive numerical demands that these models place on computational resources, the current work neglects the effects of *sgs* scalar-mixing processes and focuses on detailed treatments of thermodynamic nonidealities and transport anomalies. To account for thermodynamic nonidealities and transport anomalies over a wide range of pressures and temperatures, an extended corresponding states principle similar to that developed by Rowlinson and Watson[7] is employed using two different equations of state. The 32-term Benedict–Webb–Rubin (BWR) equation of state proposed by Jacobsen and Stewart[8] is used to predict the pressure–volume–temperature (PVT) behavior of liquid-phase, saturated-vapor, and gas-phase mixture properties in the vicinity of the critical point. The Soave–Redlich–Kwong (SRK) equation of state given by Reid et al.[9] is used elsewhere. Having established an analytical representation for the real mixture PVT behavior, explicit expressions for the enthalpy, Gibbs energy, and constant pressure specific heat are obtained as a function of temperature and pressure using Maxwell's relations to derive thermodynamic departure functions.[10] Viscosity, thermal conductivity, and the effective mass diffusion coefficients are obtained in a similar manner using the methodologies developed by Ely and Hanley[11–13] and those developed by Bird et al.,[14] Wilke and Lee,[15] Takahashi,[16] and Hayduk and Minhas,[17] respectively.

Turbulence quantities are modeled using the large-eddy-simulation (LES) technique and the *sgs* models proposed by Erlebacher et al.,[18] Speziale,[19] and Bardina et al.[20] These works employ a Favre-averaged generalization of the Smagorinsky eddy viscosity model[21] coupled with gradient diffusion models to simulate *sgs* energy and species transport processes. Spray dynamics are modeled by solving a set of Lagrangian equations of motion and transport for the life histories of a statistically significant sample of particles. Here, the stochastic-separated-flow (SSF) methodology developed by Faeth[22] is

Table 2 Hydrogen–oxygen reaction mechanism and associated forward-rate Arrhenius constants in units of m³-kmol-s-J-K[a]

No.	Reaction[b]	A_{f_j}	m_{f_j}	E_{f_j}/R_u
	H_2–O_2 chain reactions			
R1	$H + O_2 \rightleftharpoons OH + O$	8.30×10^{10}	0.00	7258
R2	$O + H_2 \rightleftharpoons OH + H$	5.00×10^{1}	2.67	3167
R3	$OH + H_2 \rightleftharpoons H_2O + H$	2.16×10^{5}	1.51	1727
R4	$OH + OH \rightleftharpoons O + H_2O$	3.57×10^{1}	2.40	−1063
	H_2–O_2 dissociation/recombination reactions			
R5	$H + H + M \rightleftharpoons H_2 + M$	1.00×10^{12}	−1.00	0
R6	$H + H + H_2 \rightleftharpoons H_2 + H_2$	9.00×10^{10}	−0.60	0
R7	$H + H + H_2O \rightleftharpoons H_2 + H_2O$	6.00×10^{13}	−1.25	0
R8	$O + O + M \rightleftharpoons O_2 + M$	1.20×10^{11}	−1.00	0
R9	$O + H + M \rightleftharpoons OH + M$	5.00×10^{11}	−1.00	0
R10	$H + OH + M \rightleftharpoons H_2O + M$	2.20×10^{16}	−2.00	0
	Formation and consumption of HO_2			
R11	$H + O_2 + M \rightleftharpoons HO_2 + M$	2.80×10^{12}	−0.86	0
R12	$H + O_2 + O_2 \rightleftharpoons HO_2 + O_2$	3.00×10^{14}	−1.72	0
R13	$H + O_2 + H_2O \rightleftharpoons HO_2 + H_2O$	9.38×10^{12}	−0.76	0
R14	$H + HO_2 \rightleftharpoons H_2 + O_2$	2.80×10^{10}	0.00	537.8
R15	$H + HO_2 \rightleftharpoons OH + OH$	1.34×10^{11}	0.00	319.8
R16	$H + HO_2 \rightleftharpoons O + H_2O$	3.97×10^{9}	0.00	337.9
R17	$O + HO_2 \rightleftharpoons OH + O_2$	2.00×10^{10}	0.00	0
R18	$OH + HO_2 \rightleftharpoons O_2 + H_2O$	2.90×10^{10}	0.00	−251.8
	Formation and consumption of H_2O_2			
R19	$OH + OH + M \rightleftharpoons H_2O_2 + M$	7.40×10^{7}	−0.37	0
R20	$HO_2 + HO_2 \rightleftharpoons O_2 + H_2O_2$	1.30×10^{8}	0.00	−820.8
R21	$H + H_2O_2 \rightleftharpoons OH + H_2O$	1.00×10^{10}	0.00	1813
R22	$H + H_2O_2 \rightleftharpoons HO_2 + H_2$	1.21×10^{4}	2.00	2619
R23	$O + H_2O_2 \rightleftharpoons HO_2 + OH$	9.63×10^{3}	2.00	2014
R24	$OH + H_2O_2 \rightleftharpoons HO_2 + H_2O$	1.75×10^{9}	0.00	161.1

[a]Forward reaction rate constants are given by the Arrhenius law $k_{f_j} = A_{f_j} T^{m_{fj}} \exp(-E_{f_j}/R_u T)$.
[b]Chaperon efficiencies employed for third-body reactions are Eq. (5), $\varepsilon_{H_2} = 0.00$, $\varepsilon_{H_2O} = 0.00$; Eq. (8), $\varepsilon_{H_2} = 2.40$, $\varepsilon_{H_2O} = 15.4$; Eq. (9), $\varepsilon_{H_2} = 2.00$, $\varepsilon_{H_2O} = 6.00$; Eq. (10), $\varepsilon_{H_2} = 0.73$, $\varepsilon_{H_2O} = 3.65$; Eq. (11), $\varepsilon_{O_2} = 0.00$, $\varepsilon_{H_2O} = 0.00$, $\varepsilon_{N_2} = 0.00$; and Eq. (19), $\varepsilon_{H_2} = 2.00$, $\varepsilon_{H_2O} = 6.00$. Species not indicated have efficiencies equal to unity.

employed, with subcritical droplet dynamics modeled using classical correlations, as summarized by Faeth,[23] and transcritical dynamics modeled using a set of correlations developed by Lafon et al.,[24] Hsiao,[25] and Hsiao et al.[26] The latter correlations quantify the dynamics of a transcritical oxygen spray undergoing a change of state in a supercritical hydrogen environment. These correlations have been summarized by Oefelein and Yang.[6]

Chemical kinetics are modeled assuming nine species (H_2, O_2, OH, H_2O, H, O, HO_2, H_2O_2, and N_2), using the 24-step reduced-mechanism optimized by Frenklach et al.[27] The reaction set and corresponding Arrhenius constants are listed in Table 2. The model includes nitrogen as an inert species and has been validated at temperatures ranging from 300 to 3000 K and at several pressures for pressure-dependent reactions. This scheme represents an extension of the 18-step mechanism proposed by Westbrook and Dryer[28] and incorporates the major findings and conclusions given by Basevich[29] and Yetter et al.[30] Using this mechanism, forward reaction rate constants are obtained as a function of the Arrhenius law. Backward rate constants are obtained quite accurately as a function of the forward rates by calculating the respective equilibrium constants.

The governing system is discretized using a preconditioned, density-based, finite volume methodology. This framework takes full account of thermodynamic nonidealities and transport anomalies and accommodates any arbitrary equation of state. Temporal discretization is obtained using second-order-accurate dual-time-stepping integration. Spatial discretization is obtained using the fourth-order-accurate flux-differencing methodologies developed by Rai and Chakravarthy[31] and a total-variation-diminishing (TVD) scheme that is evaluated using the methodologies developed by Swanson and Turkel[32] and Jorgenson and Turkel.[33] The solver employs vectorized alternating-direction-implicit (ADI) factorization,[34,35] using the convergence acceleration techniques developed by Choi and Merkle,[36] Buelow et al.,[37] Buelow,[38] and Venkateswaran and Merkle.[39]

Results and Discussion

The analyses conducted by Oefelein[5] explored a variety of issues related to appropriate theoretical and numerical treatments of transcritical and supercritical mixing and combustion processes. Case studies selected were designed to isolate the phenomena of interest while minimizing the uncertainties associated with various modeling assumptions. First, the basic issues related to model performance and accuracy were examined. Algorithmic properties were established and linear theory was employed to obtain a precise set of spatial and temporal resolution requirements. A series of numerical results were then compared to the analytical predictions to establish the accuracy of the numerical scheme in the small perturbation limit and to provide an assessment of the effects imposed by the *sgs* models relative to those imposed by numerical dissipation. The results of these studies were then applied to examine the phenomena associated with the limiting extremes depicted in Fig. 1. A total of two sets of parametric studies were conducted. The first study employed a Lagrangian–Eulerian implementation of the governing system to simulate transcritical spray dynamics in a manner consistent with the

phenomena depicted in Fig. 1a. The second employed a pure Eulerian implementation of the governing system to simulate transcritical and supercritical mixing and combustion processes in a manner consistent with the diffusion mechanism depicted in Figs. 1b and 2.

Thermophysical Trends

Figures 3 and 4 illustrate the effectiveness of the methodologies outlined earlier for predicting the thermophysical behavior of oxygen and hydrogen within the regimes of interest. Plots of density, specific heat, viscosity, and thermal conductivity are given for the interval $40 \leq T \leq 1000$ K, and for pressures of 1, 10, 50, 100, 200, and 400 atm. For oxygen, density predictions are compared in the liquid, saturated vapor, and gaseous regimes with experimentally derived values obtained by Vargaftik.[40] The average deviation between the experimental and calculated densities is less than 0.2%. These figures illustrate key trends over the range of pressures and temperatures of interest. At 1000 K and above, both oxygen and hydrogen exhibit ideal gas behavior and the pressure effect is negligible. As the temperature is decreased below 1000 K, however, significant nonidealities are introduced, with property variations associated with oxygen inducing the most significant effects.

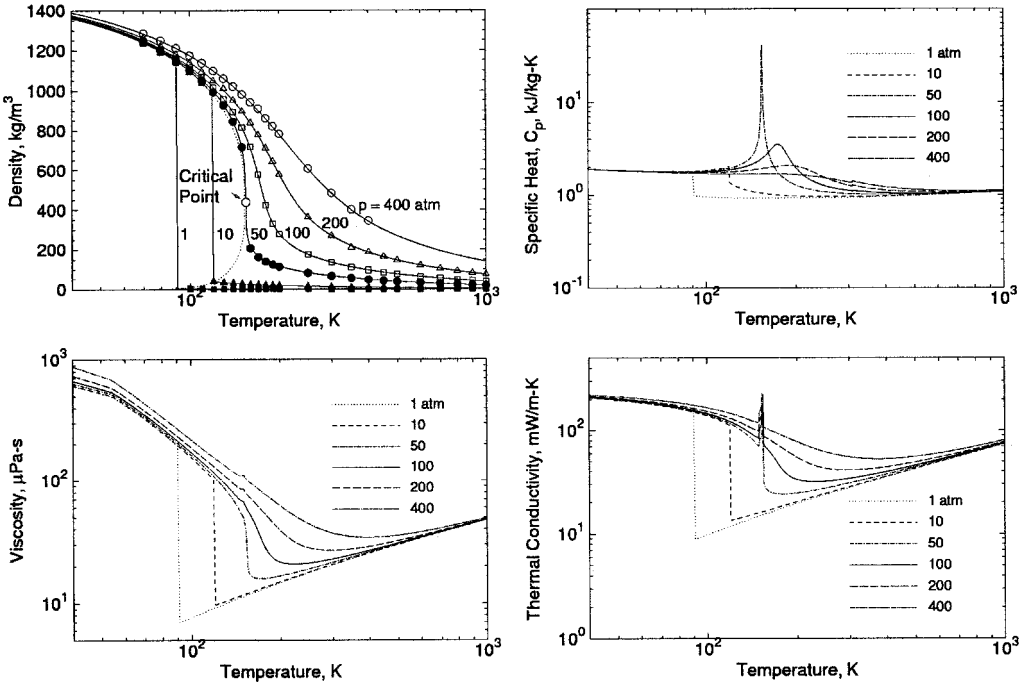

Fig. 3 Density (compared with the experimental data points obtained by Vargaftik,[40] specific heat, viscosity, and thermal conductivity vs temperature over the interval $40 \leq T \leq 1000$ K and pressures of 1, 10, 50, 100, 200, and 400 atm for pure oxygen.

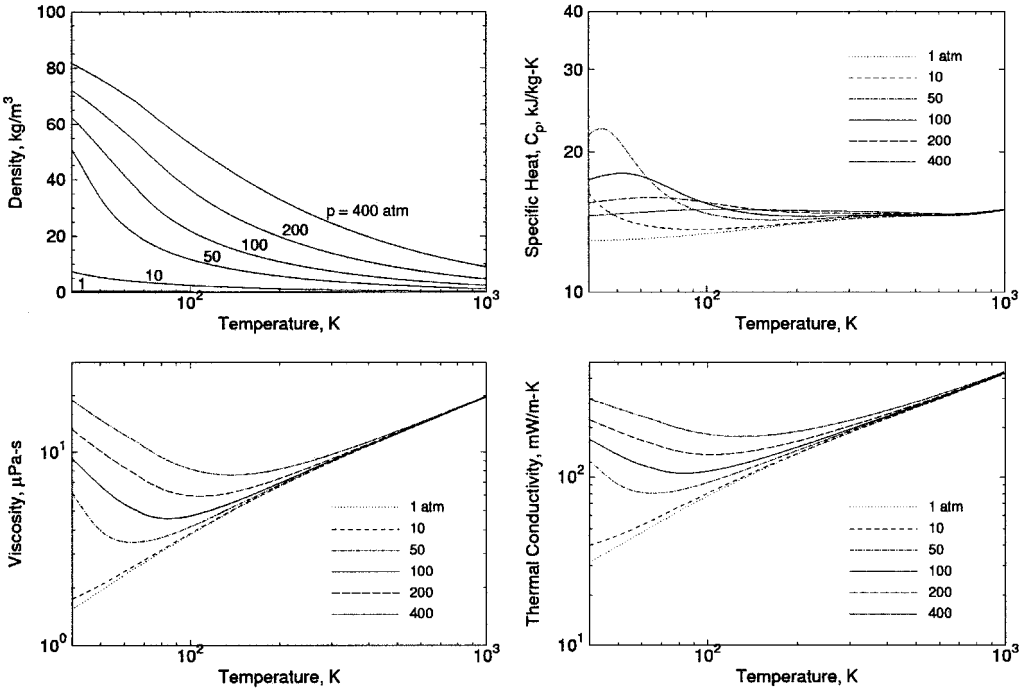

Fig. 4 Density, specific heat, viscosity, and thermal conductivity vs temperature over the interval $40 \leq T \leq 1000$ K and pressures of 1, 10, 50, 100, 200, and 400 atm for pure hydrogen.

Figure 5 shows the trends associated with the kinematic viscosity. The effect of pressure on this quantity is particularly significant and has a direct impact on the characteristic scales associated with the turbulence field. For both oxygen and hydrogen, an increase in pressure from 1 to 100 atm results in a corresponding reduction in the kinematic viscosity of up to three orders of magnitude. This implies a three-order-of-magnitude increase in the characteristic Reynolds number. Based on Kolmogorov's universal equilibrium theory,[41,42] the order of magnitude of the Kolmogorov microscale, denoted here as ν_t, and the Taylor microscale, denoted here as λ_t, are related to the Reynolds number by equations of the form

$$\frac{\eta_t}{l_t} \sim Re_t^{-3/4}, \qquad \frac{\lambda_t}{l_t} \sim Re_t^{-1/2} \tag{5}$$

Here, the Reynolds number is defined as $Re_t = q_t l_t/\nu$, where $q_t = \sqrt{2k_t/3}$. The term q_t represents the turbulence intensity, k_t the *sgs* kinetic energy, and l_t the integral length scale. The relations given by Eq. (5) indicate that a 3 order-of-magnitude decrease in the kinematic viscosity results in 2.25 and 1.5 order-of-magnitude decreases in the Kolmogorov and Taylor microscales, respectively. These reductions have a direct impact on the overall grid density required to resolve key processes.

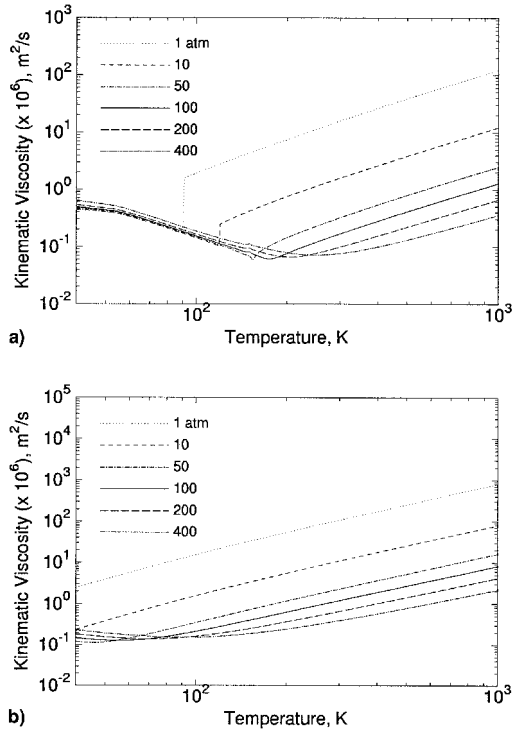

Fig. 5 Kinematic viscosity of a) pure oxygen and b) pure hydrogen over the temperature interval $40 \leq T \leq 1000$ K and pressures of 1, 10, 50, 100, 200, and 400 atm.

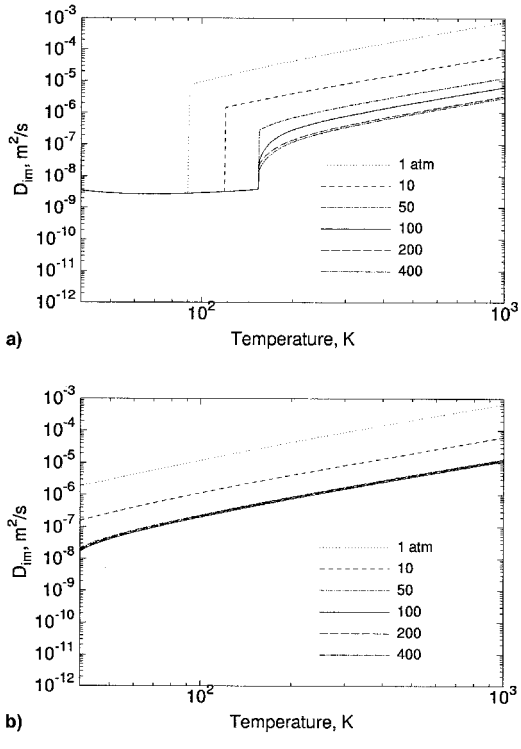

Fig. 6 Effective mass diffusivity of a) pure oxygen and b) pure hydrogen over the temperature interval $40 \leq T \leq 1000$ K and pressures of 1, 10, 50, 100, 200, and 400 atm.

Figure 6 shows the trends associated with the effective mass diffusivity. When the pressure is increased from 1 to 100 atm, oxygen and hydrogen exhibit a two-order-of-magnitude decrease in the mass diffusion rate over the full range of temperatures plotted. Oxygen exhibits a decrease of up to four orders of magnitude at temperatures below the critical mixing temperature. The diminished mass diffusion rates coupled with the liquid-like densities that dominate at high pressures significantly alter the coupling dynamics associated with local fluid dynamic and physicochemical interactions.

Algorithmic Properties

To minimize the uncertainties associated with temporal accuracy, detailed von Neumann[43] (or Fourier) stability analyses were carried out to characterize the "outer-loop" characteristics of the baseline fourth-order-accurate scheme. Unlike the pseudophysical "inner-loop" characteristics, the physical characteristics of the outer-loop must be handled in a time-accurate manner using a globally fixed time step and minimal levels of numerical dissipation and dispersion.

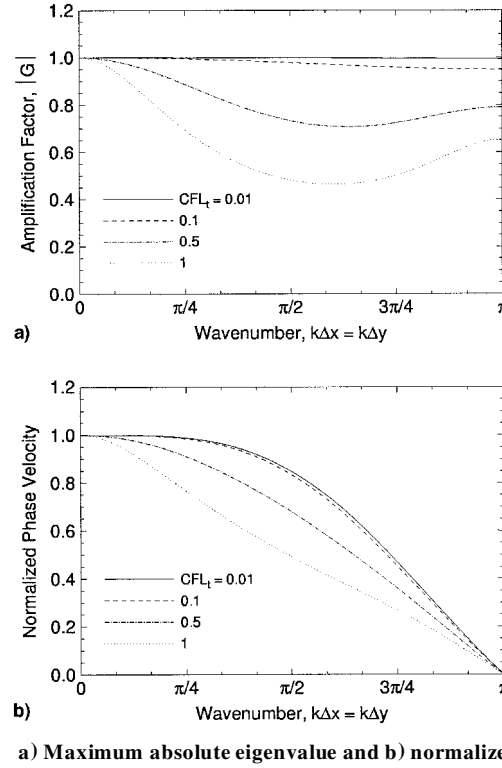

Fig. 7 a) Maximum absolute eigenvalue and b) normalized phase velocity of the outer-loop amplification matrix vs wave number $k\Delta x = k\Delta y$ and $CFL_t = 0.01, 0.1, 0.5$, and 1 for the preconditioned, fourth-order accurate, dual-time ADI scheme. CFL = 3, $\varepsilon_e = 0.25$, $\varepsilon_i = 0.25$, AR = 1, $M = 0.1$, and $v/u = 1$.

Figure 7 presents the maximum absolute eigenvalue of the outer-loop amplification factor and the corresponding phase velocities vs the wave number $k\Delta x = k\Delta y$ for Courant–Friedrichs–Lewy (CFL) numbers defined with respect to the physical-time step of $CFL_t = 0.01$, 0.1, 0.5, and 1 within a finite volume cell with an aspect ratio of 1, Mach number of 0.1, and a flow angle of 45 deg. Analysis of these plots suggests that acceptable damping and dispersion characteristics are obtained only when the grid and physical time step are specified such that local values of CFL_t are on the order of 0.1 throughout the flowfield, and not 1 as was typically assumed for dual-time systems. As local values of CFL_t approach and exceed 0.5, unacceptable levels of dissipation and dispersion are introduced. When values approach 0.01, diminished levels of dissipation at the high wave numbers can lead to instabilities in the high wave number modes.

The results presented were calculated by assuming that the pseudotime system was driven to machine accuracy, thus, the resultant trends represent a best-case scenario. If in practice the pseudotime error transients are not eliminated to an acceptable order of accuracy, the levels of dissipation and dispersion will be higher than those relative to the levels indicated in the plots. Detailed analyses[5] have demonstrated that the most restrictive flow angle is 45 deg and the least restrictive is 0 deg. Trends associated with the 45-deg flow angle indicate that the preconditioned system is less dissipative at the high wave numbers and has a negligible impact on the corresponding phase speeds. The trends associated with the 0-deg flow angle are identical to those obtained using a scalar convection equation and are independent of the preconditioning factor.

Resolution Characteristics

Linear stability theory provides an excellent standard against which to test the accuracy of a numerical scheme in the small perturbation limit. Here, the results from a series of calculations are summarized. These results demonstrate the spatial and temporal resolution required to accurately simulate the linear mechanism in a supercritical hydrogen shear layer. A schematic diagram of the computational domain is illustrated in Fig. 8. The overall length is 200 mm and the width is 50 mm. The hydrogen streams are injected at a pressure of 100 atm and a temperature of 1000 K. In all cases considered, the initial shear-layer thickness is specified as 1 mm and the inlet velocity distribution is perturbed at the fundamental frequency given by the Orr–Sommerfeld equation, with a 0.1% perturbation amplitude applied to the corresponding eigenfunctions. The axial component of the mean flow velocity is specified using a hyperbolic tangent profile, with $U_1 = 200$ m/s ($M_1 = 0.082$) and $U_2 = 50$ m/s ($M_2 = 0.021$). The transverse component of the mean flow velocity is specified as zero. Nonreflecting outflow conditions are imposed at the exit[44–46] and inviscid, adiabatic, and noncatalytic conditions are imposed at the transverse boundaries.

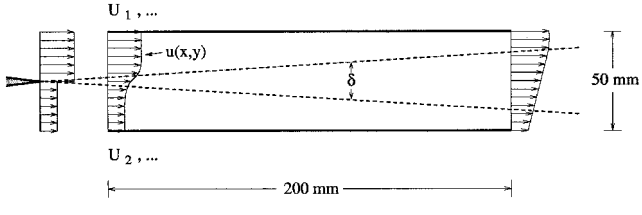

Fig. 8 Schematic diagram of the computational domain used to simulate a supercritical hydrogen shear layer. The initial shear layer thickness is 1 mm, the inlet velocity distribution is perturbed according to the fundamental mode or the fundamental and first subharmonic modes given by the Orr-Sommerfeld equation, a 0.1% perturbation amplitude is applied to the corresponding eigenfunctions, $U_1 = 200$ m/s, $U_2 = 50$ m/s, $p_{ref} = 100$ atm, $T = 1000$ K, nonreflecting outflow conditions are imposed at the exit, inviscid, adiabatic, and noncatalytic conditions are imposed at the transverse boundaries.

The velocity ratio associated with the conditions cited earlier is $U_2/U_1 = 0.25$. The corresponding Reynolds number is $Re_\delta = 2.35 \times 10^4$. Table 3 lists the characteristic frequencies and eigenvalues associated with the fundamental and first subharmonic modes for these conditions. Note that the fundamental mode imposes the most restrictive conditions. This mode exhibits the highest frequency content and the smallest wavelength. For the conditions cited, the frequency associated with the fundamental mode is 8658 Hz and the corresponding wavelength is 14.5 mm. The frequency and wavelength associated with the first subharmonic mode are 4329 Hz and 32.4 mm, respectively.

The physical time step employed for the numerical calculations was selected based on the results given by the von Neumann stability analysis outlined in the previous section. The time step and grid spacing were specified so that the average value of the local physical CFL number was on the order of 0.1 throughout the flowfield. For the conditions cited, a time step of $\Delta t = 1$ μs was required. This yielded 115 physical time steps per cycle of the fundamental mode.

The grid spacing required to accurately simulate the linear mechanism was determined by performing a parametric study using six different grids with a specified number of cells per wavelength clustered in the axial direction and a specified number of cells clustered within the shear layer in the transverse direction. Stretching was used to minimize the overall grid density required to resolve the predominant processes. The stretching factors were obtained by trial and error so that the necessary amount of clustering in the axial and transverse directions was maintained throughout the flowfield. Numerical estimates were obtained for each case by plotting the absolute value of the dimensionless centerline velocity component as a function of axial distance. When plotted on a logarithmic scale, the growth rate is clearly characterized by a linear increase in the local peak amplitudes and the corresponding wavelength is characterized by two logarithmic cycles.

For the spatially fourth-order-accurate scheme, errors of less than 2% between the numerical and analytical solutions were obtained with an axial distribution of 16 cells per wavelength and a transverse distribution of eight cells clustered within the shear layer. The grid distribution corresponding to these intervals is given by Fig. 9. The overall mesh size is 120 × 76. A stretching factor of 1.02 is employed in the axial direction.

Table 3 Characteristic frequencies and eigenvalues[a]

	Fundamental mode	First subharmonic mode
Frequency, ω	0.272	0.136
Growth rate, $-\mathcal{I}(\alpha)$	0.120	0.0872
Wave number, $\mathcal{R}(\alpha)$	0.434	0.194

[a]Given by the Orr-Sommerfeld equation for the fundamental and first subharmonic modes for a velocity ratio of $U_2/U_1 = 0.25$ and a Reynolds number of $Re_\delta = 23.5 \times 10^4$. $\omega = \Omega\delta/U_1$, $\alpha = k\delta$, where $\Omega \equiv$ angular frequency, $\delta \equiv$ initial shearlayer thickness, and $k \equiv$ wave number.

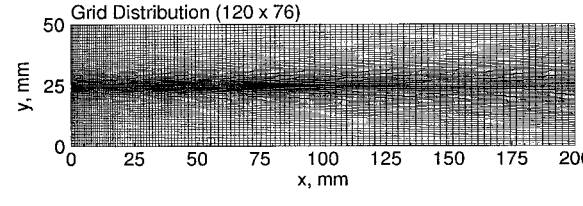

Fig. 9 Grid distribution required to resolve the fundamental and first subharmonic modes for the conditions cited in Table 3 and Fig. 8. An axial stretching factor of 1.02 is employed, transverse stretching factors of approximately 1.10 and 1.01 are employed at the inlet and exit plane, respectively.

Transverse stretching factors of 1.10 and 1.01 are specified at the inlet and exit planes, respectively.

Baseline Flow Characteristics

To examine the effects imposed by the *sgs* models relative to those imposed by numerical dissipation, the respective contributions to the residuals of the momentum equations were analyzed. The analysis was conducted using the supercritical hydrogen shear layer and the fourth-order-accurate scheme at the conditions cited in Table 3 and Fig. 8. Here, the inlet velocity was perturbed according to the fundamental and the first subharmonic modes. The calculations were performed using the resolution requirements established earlier by specifying a physical time step of 1 μs and the 120 × 76 grid given in Fig. 9.

Figure 10 shows the instantaneous pressure and vorticity fields. The pressure field is plotted in terms of a dimensionless perturbation, with p_{ref} = 100 atm. The vorticity field is normalized using the centerline vorticity at the inlet, where $\omega_{ref} = -74{,}000\ s^{-1}$. These plots illustrate the evolutionary structure of the flow. Vorticity, initially concentrated in the basic velocity profile, is redistributed into larger vortices, with wavelength doubled and frequency halved after each pairing interaction. These interactions induce peak-to-peak differences of approximately 0.50% in the nondimensional pressure field, and the vorticity distribution diffuses such that the relative core strength is decreased to a level that is approximately 45% of the initial reference value at a downstream distance of 100 mm. The corresponding velocity perturbation in the transverse direction at this location is approximately ±60 m/s.

The contributions of the numerical and *sgs* dissipation to the residual of the discretized system at the instant in time represented by Fig. 10 are shown in Fig. 11. The values plotted were extracted from the centerline of the computational domain at y = 25 mm and the interval $0 \le x/L \le 1$, where L = 200 mm. As the flow evolves spatially from the inlet, the *sgs* terms in both coordinate directions exhibit a high-amplitude growth rate that dominates over the interval $0 \le x/L \le 0.25$. Beyond this range, however, the contributions from both sources are of the same order of magnitude. The numerical dissipation tends to dominate in the axial direction and a relatively weak correlation exists between the two curves. The *sgs* dissipation tends to dominate in the transverse direction and a somewhat stronger correlation is exhibited. The trends shown here indicate that the numerical dissipation by itself behaves roughly as an *sgs* model. There is no guarantee, however, that the numerical component provides the phenomenologically correct levels of dissipation. The development of schemes with acceptable dissipation characteristics are an ongoing area of research.

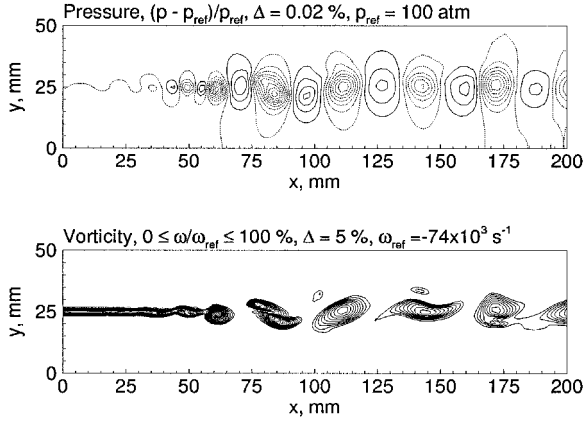

Fig. 10 Contours of the instantaneous pressure and vorticity given by the fourth-order-accurate central-difference scheme at the conditions cited in Table 3 and Fig. 8. The inlet velocity distribution is perturbed according to the fundamental and the first subharmonic modes and the 120 × 76 grid given in Fig. 9 is employed.

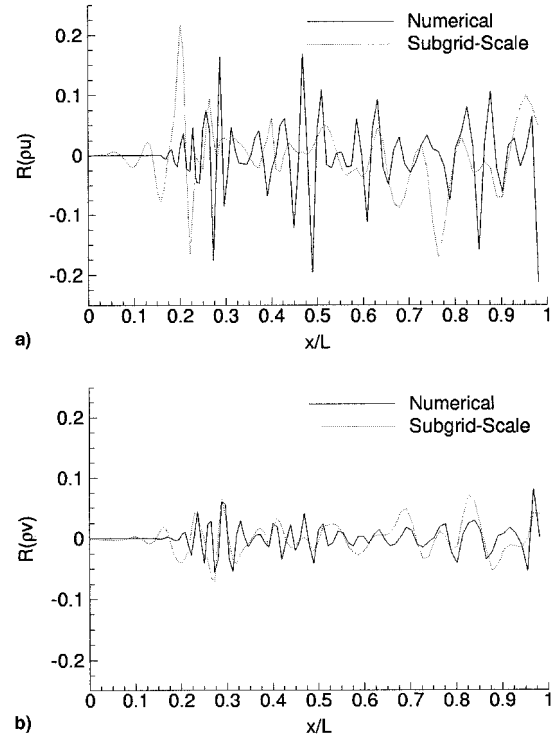

Fig. 11 Contributions to the residual a) $R(\bar{\rho}\tilde{u})$ and b) $R(\bar{\rho}\tilde{v})$ at the instant in time represented by Fig. 10. Values were extracted along the centerline of the computational domain at y = 25 mm on the interval $0 \le x/L \le 1$, where L = 200 mm.

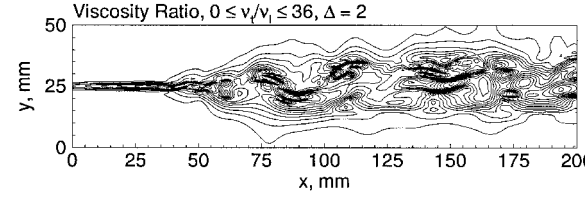

Fig. 12 Contours of the instantaneous dimensionless turbulent viscosity associated with the flowfield characterized by Fig. 10.

Figure 12 shows a contour plot of the instantaneous turbulent viscosity ratio ν_t/ν_l, where ν_t represents the turbulent eddy viscosity given by the Smagorinsky model,[21] and ν_l is the molecular kinematic viscosity. This ratio is directly proportional to the *sgs* Reynolds number and characterizes the predominance of turbulent vs molecular diffusion processes. The case shown corresponds to the flowfield presented in Fig. 10. At 100 atm, the turbulent diffusivity imposes a moderate effect on the evolutionary structure of the flow. The turbulent viscosity reaches values that are approximately 36 times greater than the molecular viscosity in regions of high shear, and values that are approximately one or two orders of magnitude smaller outside of the mixing region. The developing structures exhibit a more diffuse character in comparison to the structure obtained when no *sgs* model is employed. At lower pressures; i.e, when $Re_\delta \sim 100$, the turbulent viscosity given by the Smagorinsky model becomes much smaller than the molecular viscosity and its effect becomes negligible. As the pressure is increased to 400 atm, which for the hydrogen system yields a Reynolds number of $Re_\delta = 8.73 \times 10^4$, the viscosity ratio approaches a value of approximately 160, and the diffusivity induced by the turbulence field dominates.

High-Pressure Spray Dynamics

The Lagrangian–Eulerian calculations focus on multiphase interactions in the dilute regime depicted in Fig. 1a. Results

demonstrate the effect of large-scale structures on mixing and dispersion characteristics, the influence of *sgs* interactions, and the impact of propellant striations on the evolutionary structure of the flow. The computational domain, grid distribution, and boundary conditions specified are identical to those given in Figs. 8 and 9. The inlet velocity profile was perturbed according to the fundamental and first subharmonic modes, as given by Table 3. In addition to the 100-atm condition, pressures of 1 and 400 atm were considered and a dilute 100 K liquid-oxygen spray was injected at the trailing edge of the splitter plate. These conditions are identical to those used to obtain the high-pressure correlations.

The Lagrangian system was characterized using the Bassett, Boussinesq, and Oseen (BBO) equations[47] coupled with the stochastic-separated-flow (SSF) methodology developed by Faeth,[22] and transport equations that describe the life histories of a statistically significant sample of particles. Because of the large number of droplets present in an actual spray, the discrete particle model originally developed by Crowe et al.[48] was employed, where characteristic groups of droplets are represented by computational parcels. At each physical time step, parcels of fixed mass are injected with randomly selected diameters. These diameters are specified according to the upper limit distribution given by Fig. 13. The Sauter mean diameter associated with this distribution, D_{32}, is 100 μm, and the characteristic droplet diameter of the kth parcel is selected over the interval $0 < d_{d_k} \leq 200$ μm. The initial velocity of each parcel was assigned a value corresponding to the local instantaneous gas-phase velocity.

The cases examined are summarized in Table 4. Cases 1, 2, and 3 were selected to establish the flow characteristics of the hydrogen shear layer at 1, 100, and 400 atm with no spray injected. Cases 4–9 were selected to establish the corresponding spray characteristics as a function of pressure and the amount of oxygen injected within the shear layer. The amount of oxygen within the shear layer was quantified by means of an oxygen to hydrogen mass flow ratio defined per unit length in the spanwise direction using the shear-layer thickness at the inlet as the characteristic scale. Cases 4–6 focused on the effects of pressure when the oxygen to hydrogen mass flow ratio was held fixed at a value of 4. Case 4 provided an assessment of subcritical spray characteristics at 1 atm using classical low-pressure correlations. Cases 5 and 6 provided an assessment of transcritical spray characteristics at 100 and 400 atm, respectively. After establishing these characteristics, the pressure was held fixed at 100 atm (cases 7 and 8) and the oxygen to hydrogen mass flow ratio was varied to provide an assessment over the increments of 0, 2, 4, and 6. Case 5 provides a common link between the two data sets. The vaporization model was turned off for case 9 to assess the influence of hard spheres injected with an equivalent mass flow ratio of 4.

The conditions listed for case 2 in Table 4 are identical to those used to obtain the solution given by Figs. 10 and 12. When nondimensionalized in an identical manner, the trends exhibited by the pressure, vorticity, and velocity fields associated with cases 1–3 are essentially identical. Thus, the trends exhibited by Fig. 10 are representative of the trends exhibited for these three cases. The turbulent viscosity ratio, however, is strongly dependent on pressure. At 1 atm, the viscosity ratio ranges from 0 in the freestream to a maximum of only 0.270; thus, molecular diffusion processes dominate. Ranges of 0–36 and 0–157 are observed at 100 and 400 atm, respectively, which indicates that turbulent diffusion processes dominate at these pressures and become more pronounced with increasing pressure.

Figures 14 and 15 show the instantaneous transverse and spanwise spray distributions and the corresponding density, vorticity, and turbulent viscosity fields obtained when the baseline conditions given by case 5 are imposed using the full three-dimensional BBO equations. The conditions and instant in time shown correspond identically to those employed to obtain the solution given by Figs. 10 and 12. The instantaneous spray distributions are represented by symbols that identify respective parcel positions. The symbol size represents the characteristic droplet diameter associated with each parcel and

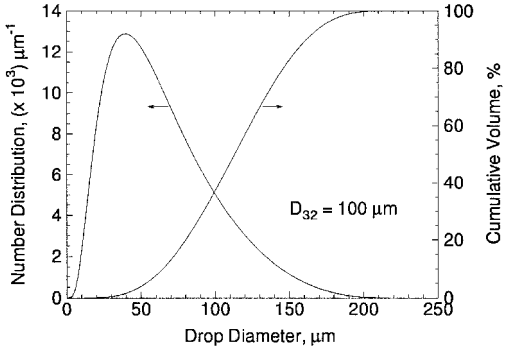

Fig. 13 Number distribution and cumulative volume of droplets injected at the inlet.

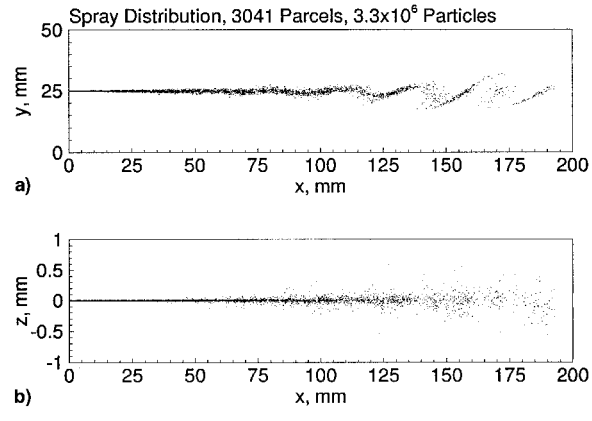

Fig. 14 Instantaneous a) transverse and b) spanwise spray field distribution associated with case 5 in Table 4.

Table 4 Inlet conditions employed for analysis of inert hydrogen-oxygen spray dynamics[a]

Case	Pressure	$\dot{m}'_{O_2}/\dot{m}'_{H_2}\|_\delta^b$	D_{32}	Notes
1	1	0	0	No spray, $Re_\delta = 2.41 \times 10^2$
2	100	0	0	No spray, $Re_\delta = 2.35 \times 10^4$
3	400	0	0	No spray, $Re_\delta = 8.73 \times 10^4$
4	1	4	100	——
5	100	4	100	Baseline conditions
6	400	4	100	——
7	100	2	100	——
8	100	6	100	——
9	100	4	100	Hard spheres

[a]Units given in atm and μm, $Re_\delta \equiv U_1\delta/\nu$.
[b]Defined using the shear-layer thickness at the inlet as the characteristic scale.

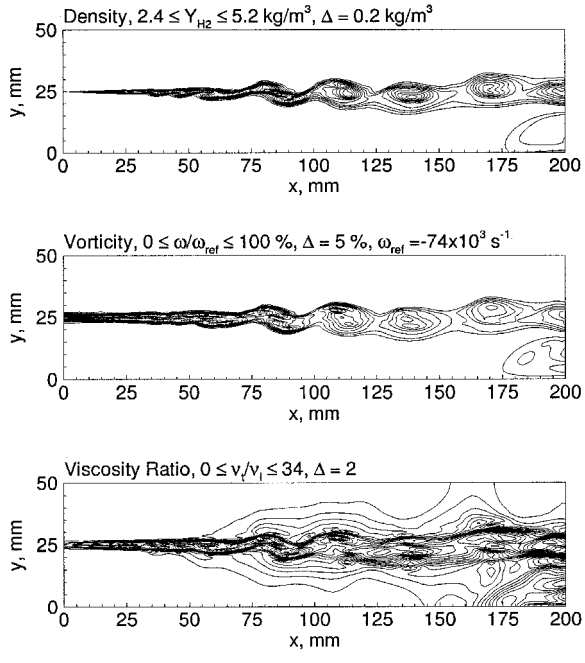

Fig. 15 Contours of the instantaneous density, vorticity, and turbulent viscosity fields associated with case 5 in Table 4.

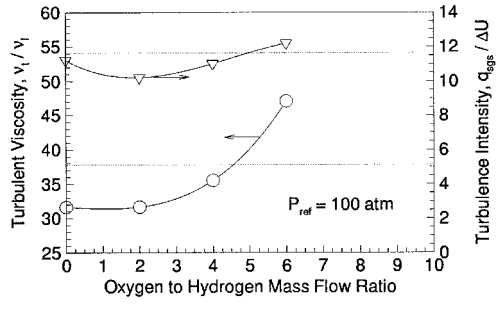

Fig. 16 Modulation of the turbulent viscosity and *sgs* turbulence intensity as a function of the oxygen to hydrogen mass flow ratio at the inlet. The dotted lines indicate respective levels exhibited with no spray injected.

is plotted to scale with respect to the grid axis. The number of parcels present in the flow domain at the instant in time shown is indicated at the top of the figure along with the total number of droplets that the parcels represent. An overview of the deviations observed with respect to the other cases is outlined next.

At 1 atm, the spray is only slightly influenced by the gas phase within the 200-mm domain. Trajectories follow an essentially straight path along the centerline and only the smallest droplets are dispersed away from the centerline. At 100 atm, as shown, the situation is markedly different. Here, droplet mixing and dispersion is dominated by the large-scale structures, and significant coupling begins at a location approximately 60 mm downstream of the inlet. Most of the droplets are completely vaporized at a downstream location of 150 mm. Similar trends are exhibited at 400 atm. For this case, however, the trends are more pronounced. Significant coupling begins approximately 45 mm downstream, and most of the droplets are completely vaporized before they reach an axial location of 80 mm downstream.

The particle field and striations of vaporized oxygen markedly alter the vorticity and turbulent viscosity fields. At equivalent instants in time, the conditions associated with cases 4–6 produce maxima in the dimensionless viscosity ratio of 0.295, 35.5, and 195, respectively. These values deviate by factors of 8.99, −6.03, and 24.8% from the values given with no spray injected. The trends observed when the pressure is fixed at 100 atm are plotted in Fig. 16. Decreasing the oxygen to hydrogen mass flow ratio to 2 yields a maximum viscosity ratio of 31.7. Eliminating the oxygen striations by turning off the vaporization model yields a maximum viscosity ratio of 31.6. Increasing the oxygen to hydrogen mass flow ratio to 6 yields a maximum viscosity ratio of 47.1. Thus, at a pressure of 100 atm, going from a condition where no striations are entrained within the mixing layer (case 9) to one where a high percentage of oxygen is entrained in the mixing layer (case 8), i.e., $\dot{m}'_{O_2}/\dot{m}'_{H_2}|_\delta$ = 0, 2, 4, and 6, yields deviations of −16.3, −16.2, −6.03, and 26.5% from the situation with no spray injected (as indicated by the dotted lines in Fig. 16). These trends can be attributed to two competing mechanisms: particle damping, and mixture-induced enhancement of turbulent diffusion processes.

In contrast to the low-pressure case, high-pressure mixing characteristics are much more sensitive to subgrid-scale fluctuations and the large-scale coherency associated with the gas phase. Gas-phase dynamics are also affected by the spray as a result of particle damping, transport between phases, and induced variations in mixture properties. Such changes alter the evolutionary structure of the flowfield. Momentum exchange between particles and the gas phase tends to damp the velocity field and reduce the level of turbulent diffusion. Elevated pressures, on the other hand, can significantly increase turbulent diffusion processes. Over the ranges considered, the change in density that accompanies increasing pressure causes the molecular kinematic viscosity to decrease significantly. This produces an overall increase in the local Reynolds number, which causes a three-order-of-magnitude increase in the normalized turbulent viscosity ratio. These effects amplify the dispersion attributes associated with the spray and markedly alter mixing and combustion processes at high pressures.

High-Pressure Mixing and Combustion Processes

The pure Eulerian calculations were fashioned after the flow visualization studies conducted by Mayer and Tamura[1] (see Fig. 2). Emphasis was placed on the near-field fluid dynamic and physicochemical processes that occur in the vicinity of the splitter plate, the impact of pressure on these processes, and the downstream flow dynamics induced as a consequence. The computational domain consists of coflowing hydrogen and oxygen streams separated by a 0.5-mm splitter plate. Inlet velocity profiles were specified assuming fully developed turbulent flow, and a heat conduction model was applied to the splitter plate to provide a realistic energy flux distribution at the walls. Conditions were specified using a reference pressure of 100 atm, with the injection temperatures selected to produce an optimal matrix of transcritical and supercritical conditions.

A schematic diagram of the computational domain is illustrated in Fig. 17. Because of the stringent numerical demands, the overall length of the domain is fixed at 10 mm and the width is 5 mm. Coflowing hydrogen (upper) and oxygen (lower) streams are injected at the inlet and separated by a 2.5 × 0.5 mm splitter plate. The heat conduction model was applied assuming Haynes-188 stainless steel to provide a realistic energy flux distribution at the walls. Velocity, temperature, and species profiles were specified at the inlet assuming fully de-

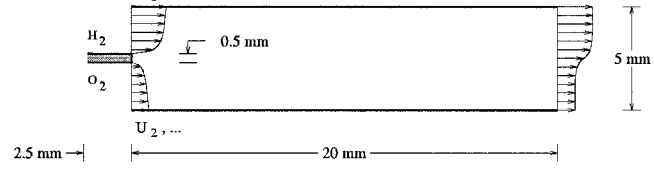

Fig. 17 Schematic diagram of the computational domain employed for the analysis of high-pressure hydrogen–oxygen mixing and combustion processes.

Table 5 Inlet conditions employed for the analysis of high-pressure hydrogen–oxygen mixing and combustion processes[a]

	Inlet Conditions					
	1	2	3	4	5	6
p, atm	100	100	100	100	100	100
T_1, K	150	150	150	300	300	300
T_2, K	100	100	100	300	300	300
T_2/T_1	0.6667	0.6667	0.6667	1	1	1
ρ_1, kg/m^3	15.37	15.37	15.37	7.752	7.752	7.752
ρ_2, kg/m^3	1118	1118	1118	134.7	134.7	134.7
ρ_2/ρ_1	72.75	72.75	72.75	17.37	17.37	17.37
U_1, m/s	500	250	125	250	125	62.5
U_2, m/s	30	30	30	30	30	30
U_2/U_1	0.06	0.12	0.24	0.12	0.24	0.48
ρ_2U_2/ρ_1U_1	4.365	8.730	17.46	2.084	4.169	8.338
$\rho_2U_2^2/\rho_1U_1^2$	0.2619	1.048	4.190	0.2501	1.001	4.002
M_1	0.4828	0.2414	0.1207	0.1786	0.08931	0.04465
M_2	0.04572	0.04572	0.04572	0.09203	0.09203	0.09203
Re_{δ_1}	1,424,000	715,700	359,400	243,200	121,900	60,990
Re_{δ_2}	245,000	245,000	245,000	201,700	201,700	201,700
Pr_1	0.7842	0.7842	0.7842	0.6913	0.6913	0.6913
Pr_2	1.917	1.917	1.917	0.7832	0.7832	0.7832
Sc_1	1.560	1.560	1.560	1.365	1.365	1.365
Sc_2	89.09	89.09	89.09	0.2207	0.2207	0.2207
Le_1	1.964	1.964	1.964	1.975	1.975	1.975
Le_2	46.48	46.48	46.48	0.2817	0.2817	0.2817

[a]Subscript 1 denotes the hydrogen stream, subscript 2 denotes the oxygen stream. $Re_\delta \equiv U_e\delta/\nu$, where U_e represents the edge velocity and δ the channel half-width.

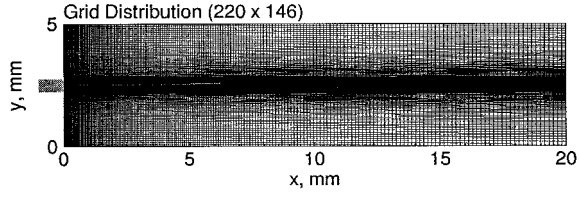

Fig. 18 Grid distribution employed for the analysis of high-pressure hydrogen–oxygen mixing and combustion processes. An axial stretching factor of 1.015 is specified. Transverse stretching factors within the boundary layer and splitter plate are 1.075, transverse stretching factors at the exit are 1.057.

Table 6 Wall coordinate y^+ values of the first grid point off the wall for the grid given in Fig. 18

	Wall coordinate values					
	1	2	3	4	5	6
Hydrogen side	146	78	41	29	15	8
Oxygen side	29	29	29	24	24	24

veloped turbulent flow. Nonreflecting outflow conditions were imposed at the exit, and inviscid, adiabatic, and noncatalytic conditions were imposed at the transverse boundaries.

In all of the cases considered, a reference pressure of 100 atm was employed and the injection temperatures and velocities were varied to obtain a representative and comparable set of thermophysical and fluid dynamic characteristics. Six different inlet conditions were examined. The relevant parameters associated with these conditions are summarized in Table 5. Conditions 1–3 provide a set of thermophysical conditions similar to those employed by Mayer and Tamura.[1] Hydrogen and oxygen injection temperatures of $T_1 = 150$ K and $T_2 = 100$ K are specified to produce a supercritical hydrogen stream and a liquid oxygen stream that undergoes a transcritical change of state within the mixing layer (see Table 1). The corresponding oxygen to hydrogen density ratio is $\rho_2/\rho_1 = 72.75$. Conditions 4, 5, and 6 provide supercritical conditions within both streams. For these cases hydrogen and oxygen injection temperatures of $T_1 = T_2 = 300$ K are specified to produce an oxygen to hydrogen density ratio of $\rho_2/\rho_1 = 17.37$.

Three factors must be considered when selecting the hydrogen and oxygen injection velocities: 1) it is desirable to specify mass flux rates typically employed in practical systems, 2) it is desirable to minimize respective Reynolds numbers and thus maximize the spatial increments associated with the characteristic turbulence scales, and 3) it is desirable to maximize the oxygen to hydrogen velocity ratio and thus minimize the spatial growth rates associated with the mixing layer downstream of the splitter plate. The quantities tabulated in Table 5 produce low-speed subsonic flow with inlet Mach numbers on the order of 10^{-1} and Reynolds numbers, as defined in Table 5, on the order of 10^5. Conditions 1, 2, and 3 employ hydrogen injection velocities of $U_1 = 500$, 250, and 125 m/s, respectively. Conditions 4, 5, and 6 employ hydrogen injection velocities of $U_1 = 250$, 125, and 62.5 m/s, respectively. An oxygen injection velocity of $U_2 = 30$ m/s is employed in all cases. This combination yields oxygen to hydrogen mass flux ratios of 4.365, 8.730, and 17.46 for conditions 1–3, and oxygen to hydrogen mass flux ratios of 2.084, 4.169, and 8.338 for conditions 4–6. The oxygen to hydrogen momentum flux ratios are 0.25, 1, and 4 for both sets of thermophysical conditions.

The grid distribution employed for all cases is given in Fig. 18. The overall mesh size is 220×146, and an optimal combination of stretching is employed to minimize the overall grid density required to resolve the predominant processes. This combination was arrived at by applying the resolution requirements established in the previous section. The grid is constructed so that 20 cells per wavelength are available, on average, to resolve the vortical structures that shed off the trailing edge of the splitter plate, and so that eight cells, on average, are clustered within the resultant shear layer. There are 41 cells clustered within the splitter plate interval in the transverse direction. An axial stretching factor of 1.015 is specified, transverse stretching factors within the boundary layer and splitter plate are 1.075, and the transverse stretching factors at the exit are 1.057.

At 100 atm, the spatial increments associated with y^+ values in the vicinity of the splitter plate range from 0.025 μm (the hydrogen stream associated with inlet condition 1) to 0.5 μm (the hydrogen stream associated with inlet condition 6). The grids required to resolve these scales are impractical. To overcome this difficulty, a wall function approach is employed and

the turbulence mixing length defined by the LES framework is scaled using the damping factor recommended by Piomelli et al.[49,50] Table 6 lists the respective y^+ values of the first grid point off the wall for the cases given in Table 5 and the grid given by Fig. 18. These coordinates demonstrate the potential limitations of the LES methodology when used to model turbulent flows at realistic chamber pressures.

Representative results are given in Figs. 19–22. Figure 19 shows the instantaneous density, temperature, velocity, and vorticity fields associated with case 3 in Table 5. Figure 20 shows the corresponding H_2, O_2, H_2O, and OH mass fraction fields. Figures 21 and 22 present the corresponding plots for case 5. The solutions shown provide a comparison between transcritical and supercritical mixing in the near field when respective hydrogen and oxygen streams are injected at identical velocities.

Transcritical mixing induces a vortical structure within the injected hydrogen stream that is analogous to that produced by a backward-facing step. This structure emanates from the upper corner of the splitter plate and coalesces downstream with adjacent vortices. The oxygen stream, on the other hand, exhibits no noticeable structure and proceeds unimpeded in an essentially straight line. Because of the liquid-like characteristics of the oxygen stream, an extremely large-density gradient exists within this region. Diminished mass diffusion rates are also evident. The combined effect produces a flame that behaves in a qualitatively similar manner as that depicted in Fig. 2. Combustion occurs at near stoichiometric conditions and

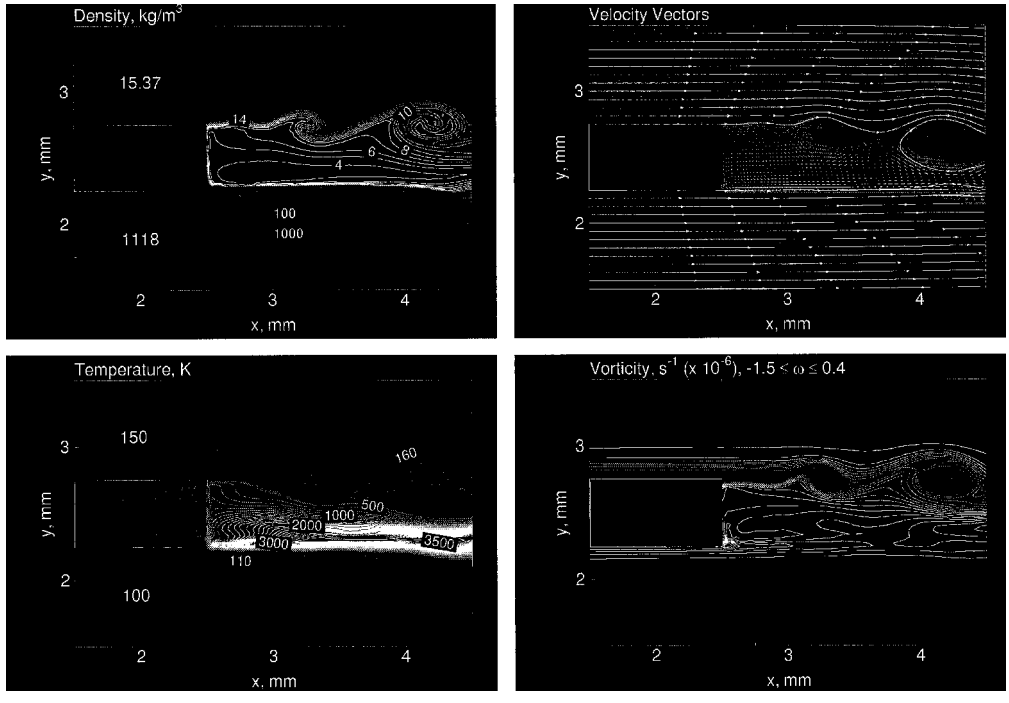

Fig. 19 Contours of density, temperature, velocity, and vorticity in the near-field region of the splitter plate for inlet condition 3 in Table 5.

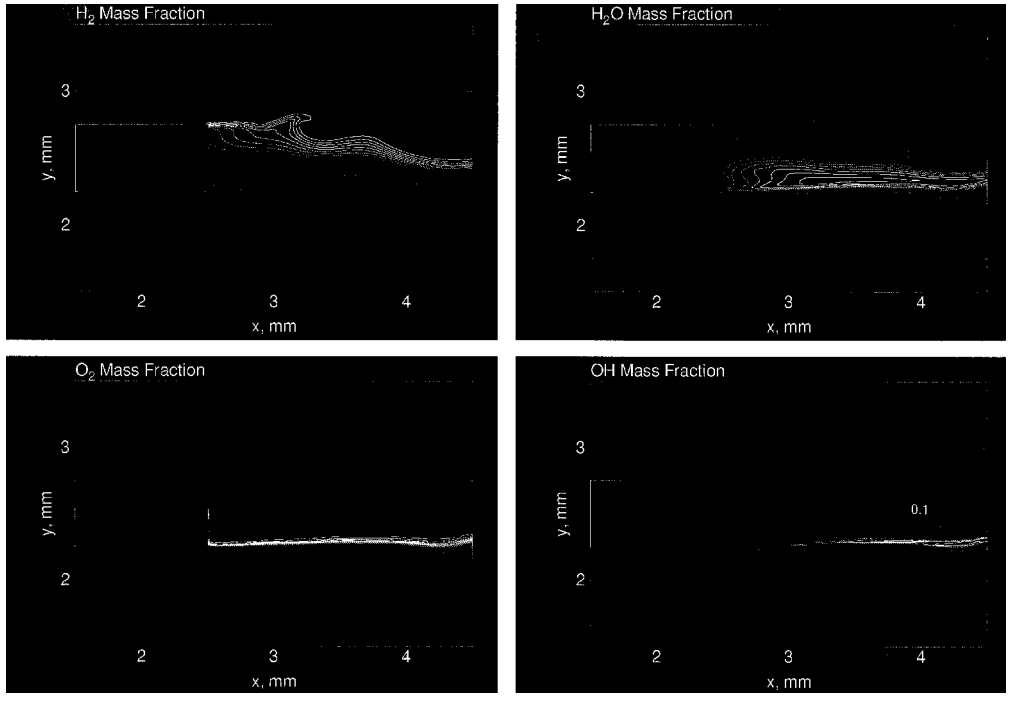

Fig. 20 Contours of H_2, O_2, H_2O, and OH mass fraction in the near-field region of the splitter plate for inlet condition 3 in Table 5.

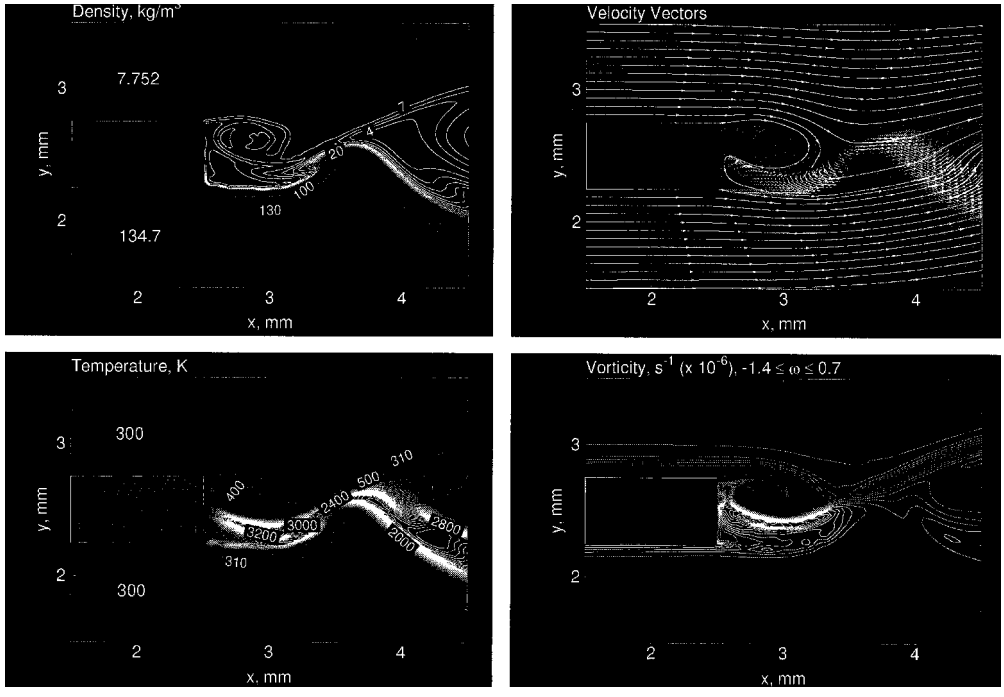

Fig. 21 Contours of density, temperature, velocity, and vorticity in the near-field region of the splitter plate for inlet condition 5 in Table 5.

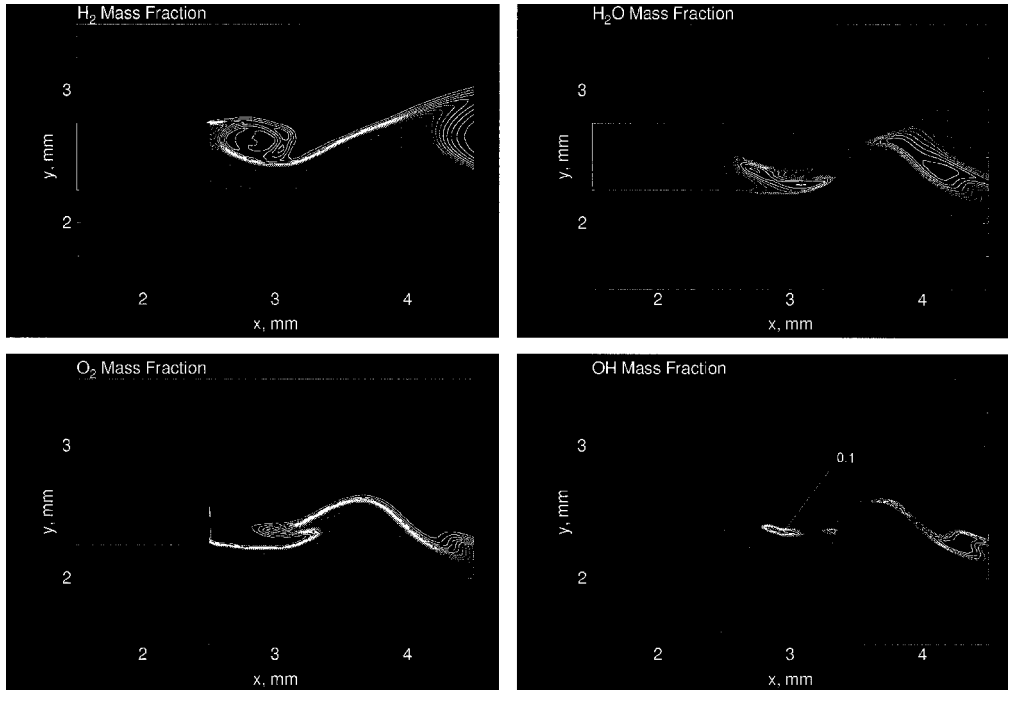

Fig. 22 Contours of H_2, O_2, H_2O, and OH mass fraction in the near-field region of the splitter plate for inlet condition 5 in Table 5.

produces a wake that effectively separates the hydrogen and oxygen streams as the flow evolves downstream.

A one-to-one comparison between Figs. 19 and 21, and 20 and 22, respectively, highlight the wide disparities that exist between transcritical and supercritical fluid dynamic and physicochemical interactions. In contrast to the transcritical situation, relatively strong vortical interactions are prevalent between the oxygen and hydrogen streams at pure supercritical conditions. The resultant interactions cause disturbances that grow and coalesce immediately downstream of the splitter plate on a scale that is of the same order of magnitude as the splitter plate thickness. Combined effects induce increased unsteadiness with respect to the flame-holding mechanism and produce significant oscillations in the production rates of H_2O and OH radicals. The temperature within the recirculation zone also fluctuates about the stoichiometric value, with relatively cooler temperatures observed immediately downstream.

Results here highlight the effect of the momentum flux ratio on flame-holding dynamics, the dominating effect of the density gradient, and the impact of diminished mass diffusion rates that accompany the liquid-like behavior of near-critical fluids. The size of the density gradient associated with transcritical injection raises concerns about numerical dissipation and the use of a pure Eulerian approach downstream of the near-field injection region. The results also demonstrate the strengths and potential limitations of the LES methodology, the primary limitation being the grid spacing required to obtain the correct limiting behavior locally between the resolved scales and *sgs*.

Summary

The results presented here demonstrate model performance and accuracy requirements, highlight various intricacies associated with transcritical and supercritical phenomena, highlight the effect of pressure on near-critical mixing and combustion processes, and provide increased insights into the theoretical and numerical methodologies employed. Results also demonstrate the dominating effect of the density gradient and diminished mass diffusion rates that accompany the liquid-like behavior of near-critical fluids.

The overall model requires improvement in terms of generality, the treatment of scalar mixing processes, and the treatment of interface dynamics. In all cases considered, the resolved-scale chemical source terms have been approximated using resolved field quantities only, with the effects of *sgs* fluctuations neglected. Such an assumption is valid only for cases in which reactions are slow relative to the time scales associated with the decay of the species fluctuations. This situation is rarely the case in contemporary combustors, and becomes decreasingly valid with increasing pressure. The use of gradient diffusion terms to model turbulence species transport is also questionable, because of the effect of heat release on the subgrid-scale turbulence field.

Acknowledgments

This manuscript summarizes a portion of the work performed independently by the first author under the NASA Marshall Space Flight Center Graduate Student Researchers Program, grant numbers NGT-50953 and NGT-51119. The support and encouragement of Charles F. Schafer and the financial support provided by this program is greatly appreciated.

References

[1]Mayer, W., and Tamura, H., "Propellant Injection in a Liquid Oxygen/Gaseous Hydrogen Rocket Engine," *Journal of Propulsion and Power*, Vol. 12, 1996, pp. 1137–1147.

[2]Hutt, J. J., and Cramer, J. M., "Advanced Rocket Injector Development at Marshall Space Flight Center," AIAA Paper 96-4266, Sept. 1996.

[3]Mayer, W., Schik, A., Schweitzer, C., and Schaffler, M., "Injection and Mixing Processes in High Pressure LOX/GH2 Rocket Combustors," AIAA Paper 96-2620, July 1996.

[4]Woodward, R. D., and Talley, D. G., "Raman Imaging of Transcritical Cryogenic Propellants," AIAA Paper 96-0468, Jan. 1996.

[5]Oefelein, J. C., "Simulation and Analysis of Turbulent Multiphase Combustion Processes at High Pressures," Ph.D. Dissertation, Pennsylvania State Univ., University Park, PA, 1997.

[6]Oefelein, J. C., and Yang, V., "Simulation of High-Pressure Spray Field Dynamics," *Recent Advances in Spray Combustion (Book II)*, edited by K. K. Kuo, Vol. 171, Progress in Astronautics and Aeronautics, AIAA, Washington, DC, 1996, pp. 263–304, Chap. 11.

[7]Rowlinson, J. S., and Watson, I. D., "The Prediction of the Thermodynamic Properties of Fluids and Fluid Mixtures—I. The Principle of Corresponding States and its Extensions," *Chemistry and Engineering Science*, Vol. 24, No. 8, 1969, pp. 1565–1574.

[8]Jacobsen, R. T., and Stewart, R. B., "Thermodynamic Properties of Nitrogen Including Liquid and Vapor Phases from 63K to 2000K with Pressure to 10,000 bar," *Journal of Physical and Chemical Reference Data*, Vol. 2, No. 4, 1973, pp. 757–922.

[9]Reid, R. C., Prausnitz, J. M., and Poling, B. E., *The Properties of Gases and Liquids*, 4th ed. McGraw–Hill, New York, 1987.

[10]VanWylen, G. J., and Sonntag, R. E., *Fundamentals of Classical Thermodynamics*, Wiley, New York, 1986.

[11]Ely, J. F., and Hanley, H. J. M., "An Enskog Correction for Size and Mass Difference Effects in Mixture Viscosity Predictions," *Journal of Research of the National Bureau of Standards*, Vol. 86, No. 6, 1981, pp. 597–604.

[12]Ely, J. F., and Hanley, H. J. M., "Predictions of Transport Properties. 1. Viscosity of Fluids and Mixtures," *Industrial and Engineering Chemistry Fundamentals*, Vol. 20, No. 4, 1981, pp. 323–332.

[13]Ely, J. F., and Hanley, H. J. M., "Predictions of Transport Properties. 2. Thermal Conductivity of Pure Fluids and Mixtures," *Industrial and Engineering Chemistry Fundamentals*, Vol. 22, No. 4, 1981, pp. 90–97.

[14]Bird, R. B., Stewart, W. E., and Lightfoot, E. N., *Transport Phenomena*, Wiley, New York, 1960.

[15]Wilke, C. R., and Lee, C. Y., "Estimation of Diffusion Coefficients for Gases and Vapors," *Industrial Engineering Chemistry*, Vol. 47, 1955, pp. 1253–1257.

[16]Takahashi, S., "Preparation of a Generalized Chart for the Diffusion Coefficients of Gases at High Pressures," *Journal of Chemical Engineering (Japan)*, Vol. 7, No. 6, 1974, pp. 417–420.

[17]Hayduk, W., and Minhas, B. S., "Correlations for Prediction of Molecular Diffusivities in Liquid," *Canadian Journal of Chemical Engineering*, Vol. 60, 1982, pp. 295–299.

[18]Erlebacher, G., Hussaini, M. Y., Speziale, C. G., and Zang, T. A., "Toward the Large Eddy Simulation of Compressible Turbulent Flows," *Journal of Fluid Mechanics*, Vol. 238, 1992, pp. 155–185.

[19]Speziale, C. G., "Galilean Invariance of Subgrid-Scale Stress Models in the Large Eddy Simulation of Turbulence," *Journal of Fluid Mechanics*, Vol. 156, 1985, pp. 52–62.

[20]Bardina, J., Ferziger, J. H., and Reynolds, W. C., "Improved Subgrid Scale Models Based on Large Eddy Simulation of Homogeneous, Incompressible, Turbulent Flows," Stanford Univ., TF-19, Stanford, CA, 1983.

[21]Smagorinsky, J., "General Circulation Experiments with the Primitive Equations. I. The Basic Experiment," *Monthly Weather Review*, Vol. 91, 1963, pp. 99–164.

[22]Faeth, G. M., "Mixing, Transport, and Combustion in Sprays," *Progress in Energy and Combustion Science*, Vol. 13, 1987, pp. 293–345.

[23]Faeth, G. M., "Evaporation and Combustion of Sprays," *Progress in Energy and Combustion Science*, Vol. 9, 1983, p. 1–76.

[24]Lafon, P., Yang, V., and Habiballah, M., "Supercritical Vaporization of Liquid Oxygen Droplet in Hydrogen and Water Environments," *Journal of Fluid Mechanics* (submitted for publication).

[25]Hsiao, C. C., "Droplet Vaporization and Combustion in Quiescent and Forced-Convective Environments," Ph.D. Dissertation, Pennsylvania State Univ., University Park, PA, 1995.

[26]Hsiao, C. C., Yang, V., and Shuen, J. S., "Vaporization of Liquid Oxygen Droplets in a Supercritical Hydrogen Stream," *Journal of Fluid Mechanics* (submitted for publication).

[27]Frenklach, M., Wang, H., Goldenberg, M., Smith, G. P., Golden, D. M., Bowman, C. T., Hanson, R. K., Gardiner, W. C., and Lissianski, V., "GRI-Mech — An Optimized Detailed Chemical Reaction Mechanism for Methane Combustion," Gas Research Inst. GRI-95/0058, 1995.

[28]Westbrook, C. K., and Dryer, F. L., "Chemical Kinetics Modeling of Hydrocarbon Combustion," *Progress in Energy and Combustion Science*, Vol. 10, 1984, pp. 1–57.

[29]Basevich, V. Y., "Chemical Kinetics in the Combustion Processes: A Detailed Kinetics Mechanism and its Implementation," *Progress in Energy and Combustion Science*, Vol. 13, 1987, pp. 199–248.

[30]Yetter, R. A., Dryer, F. L., and Rabitz, H., "A Comprehensive Reaction Mechanism for Carbon Monoxide/Hydrogen/Oxygen Kinetics," *Combustion Science and Technology*, Vol. 79, 1991, pp. 97–128.

[31]Rai, M. M., and Chakravarthy, S., "Conservative High-Order Accurate Finite-Difference Methods for Curvilinear Grids," AIAA Paper 93-3380, July 1993.

[32]Swanson, R. C., and Turkel, E., "On Central-Difference and Upwind Schemes," *Journal of Computational Physics*, Vol. 101, 1992, pp. 292–306.

[33]Jorgenson, P., and Turkel, E., "Central Difference TVD Schemes for Time Dependent and Steady State Problems," *Journal of Computational Physics*, Vol. 107, 1993, pp. 297–308.

[34]Douglas, J., and Gunn, J. E., "A General Formulation of Alternating Direction Method—Part I—Parabolic and Hyperbolic Problem," *Numerische Mathematik*, Vol. 82, 1964, pp. 428–453.

[35]Briley, W. R., and McDonald, H., "Solution of the Multidimensional Compressible Navier-Stokes Equations by a Generalized Implicit Method," *Journal of Computational Physics*, Vol. 24, 1977, pp. 372–397.

[36]Choi, Y. H., and Merkle, C. L., "The Application of Preconditioning in Viscous Flows," *Journal of Computational Physics*, Vol. 105, 1993, pp. 207–223.

[37]Buelow, P. E. O., Venkateswaran, S., and Merkle, C. L., "Effect of Grid Aspect Ratio on Convergence," *AIAA Journal*, Vol. 32, No. 12, 1994, pp. 2401–2408.

[38]Buelow, P. E. O., "Convergence Enhancement of Euler and Navier-Stokes Algorithms," Ph.D. Dissertation, Pennsylvania State Univ., University Park, PA, 1995.

[39]Venkateswaran, S., and Merkle, C. L., "Dual Time Stepping and Preconditioning for Unsteady Computations," AIAA Paper 95-0078, Jan. 1995.

[40]Vargaftik, N. B., *Tables on the Thermophysical Properties of Liquids and Gases*, 2nd ed., Wiley, New York, 1975.

[41]Tennekes, H., and Lumley, J. L., *A First Course in Turbulence*, MIT Press, Cambridge, MA, 1972.

[42]Hinze, J. O., *Turbulence*, 2nd ed. McGraw–Hill, New York, 1975.

[43]Richtmyer, R. D., and Morton, K. W., *Difference Methods for Initial-Value Problems*, Wiley, New York, 1967.

[44]Rudy, D. H., and Strikwerda, J. C., "A Nonreflecting Outflow Boundary Condition for Subsonic Navier-Stokes Calculations," *Journal of Computational Physics*, Vol. 36, 1980, pp. 55–70.

[45]Poinsot, T. J., and Lele, S. K., "Boundary Conditions for Direct Simulation of Compressible Viscous Flows," *Journal of Computational Physics*, Vol. 101, 1992, pp. 104–129.

[46]Baum, M., Poinsot, T., and Thevenin, D., "Accurate Boundary Conditions for Multicomponent Reactive Flows," *Journal of Computational Physics*, Vol. 116, 1994, pp. 247–261.

[47]Soo, S. L., *Particulates and Continuum Multiphase Fluid Dynamics*, Hemisphere, New York, 1989.

[48]Crowe, C. T., Sharma, M. P., and Stock, D. E., "The Particle-Source-In-Cell (PSI-CELL) Model for Gas-Droplet Flows," *Journal of Fluids Engineering*, Vol. 99, 1977, pp. 325–332.

[49]Piomelli, U., Ferziger, J. H., and Moin, P., "Models for Large Eddy Simulation of Turbulent Channel Flow Including Transpiration," Dept. of Mechanical Engineering, Stanford Univ., TF-32, Stanford, CA, 1988.

[50]Piomelli, U., Ferziger, J. H., Moin, P., and Kim, J., "New Approximate Boundary Conditions for Large Eddy Simulations of Wall-Bounded Flows," *Physics of Fluids*, Vol. 1, No. 6, 1989, pp. 1061–1068.

Color reproductions courtesy of Pennsylvania State University.